Computers in Biology and Medicine 114 (2019) 103454

Contents lists available at ScienceDirect

Computers in Biology and Medicine

journal homepage: www.elsevier.com/locate/compbiomed

Performance assessment of displacement-field estimation of the human left atrium from 4D-CT images using the coherent point drift algorithm

Tomohiro Otani [a,*], Mikio Shiga [b], Shunsuke Endo [c], Shigeo Wada [a]

[a] Department of Mechanical Science and Bioengineering, Graduate School of Engineering Science, Osaka University, 1-3 Machikaneyamacho, Toyonaka, Osaka, 560-8531, Japan
[b] Department of Systems Science, School of Engineering Science, Osaka University, 1-3 Machikaneyamacho, Toyonaka, Osaka, 560-8531, Japan
[c] Department of Thoracic and Cardiovascular Surgery, Jichi Medical University, 3311-1 Yakushiji, Shimotsuke, Tochigi, 329-0498, Japan

ARTICLE INFO

Keywords:
Left atrium
Four-dimensional computed tomography (4D-CT)
Displacement-field estimation
Coherent point drift (CPD)
Point set alignment

ABSTRACT

Background: Cardiac four-dimensional computed tomography (4D-CT) imaging is a standard approach used to visualize left atrium (LA) deformation for clinical diagnosis. However, the quantitative evaluation of LA deformation from 4D-CT images is still a challenging task. We assess the performance of LA displacement-field estimation from 4D-CT images using the coherent point drift (CPD) algorithm, which is a robust point set alignment method based on the expectation–maximization (EM) algorithm.

Method: Subject-specific LA surfaces at 20 phases/cardiac cycles were reconstructed from 4D-CT images and expressed as sets of triangular elements. The LA surface at the phase that maximized the LA surface area was assigned as the control LA surface and those at the other 19 phases were assigned as observed LA surfaces. The LA displacement-field was estimated by solving the alignment between the control and observation LA surfaces using CPD.

Results: Global correspondences between the estimated and observed LA surfaces were successfully confirmed by quantitative evaluations using the Dice similarity coefficient and differences of surface area for all phases. The surface distances between the estimated and observed LA surfaces ranged within 2 mm, except at the left atrial appendage and boundaries, where incomplete data, such as missing or false detections, were included on the observed LA surface. We confirmed that the estimated LA surface displacement and its spatial distribution were anisotropic, which is consistent with existing clinical observations.

Conclusion: These results highlight that the LA displacement field estimated by CPD robustly tracks global LA surface deformation observed in 4D-CT images.

1. Introduction

The left atrium (LA) is the left-upper heart chamber and transports oxygenated blood from pulmonary veins (PVs) to the left ventricle (LV) through the mitral valve (MV). The LA actively functions to modulate LV filling [1]. LA pathologic remodeling, such as LA enlargement, dysfunction and atrial fibrillation, are known risk markers that induce thrombus formation in the LA, which is associated with thromboembolic stroke [2–4]. Therefore, the assessment of subject-specific LA size and deformation has attracted much interest as a way of understanding LA performance and the risk of ischemic stroke.

Electrocardiogram-gated cardiac computed tomography (CT) is one of the most standard noninvasive methods for visualizing the three-dimensional (3D) LA shape and its deformation. Cardiac CT scanning over several cardiac cycles using a high temporal resolution multi-detector CT system yields the cardiovascular shape as volumetric image data at various cardiac phase points by synchronizing with the electrocardiogram [5]. These four-dimensional CT (4D-CT) image data allow us to visualize spatiotemporal changes in the LA surface shape. However, because the LA shape is implicitly represented as image data and there are no material points for explicitly tracking motion, kinematically exact LA wall deformation cannot be identified directly from 4D-CT images.

Cardiac motion estimation using medical imaging analysis based on the non-rigid image registration approach has been applied widely for the assessment of cardiac function from medical images, such as 4D-CT, magnetic resonance imaging, and echocardiography [6–8]. In particular, LV function is strongly associated with the risk of cardiovascular diseases, which has led to a great deal of research interest in LV function assessment. Several techniques for the assessment of LV function, such as LV spatio-temporal motion [9] and LV strain [10],

---

* Corresponding author.
E-mail address: otani@me.es.osaka-u.ac.jp (T. Otani).

https://doi.org/10.1016/j.compbiomed.2019.103454
Received 17 May 2019; Received in revised form 15 September 2019; Accepted 15 September 2019

have been developed based on medical image registration analysis, whereas less attention has been paid to the LA function, and LA image registration analyses have been reported in limited cases [11,12]. The LA myocardial wall is relatively thin, which makes imaging analysis of LA motion difficult. Moreover, complexities of LA shapes and subject-specific differences, particularly in the left atrial appendage (LAA) [13], make even LA segmentation from medical images difficult. Although several recent studies have attempted to develop automatic LA segmentation from medical images [14,15], 3D LA motion estimation using image registration remains challenging.

To overcome this issue, LA motion estimation based on LA surface registration extracted from image data may be a better alternative to direct image registration. One of the main concepts used to estimate the displacement field from image data is to describe this problem as the alignment of two point sets (point set registration), which are extracted from the outline surface of the target object in image data at different time phase points [16–19]. The coherent point drift (CPD) algorithm is an effective method that follows this concept, and was originally proposed in [18]. In the CPD algorithm, two point sets are aligned by solving a probability density estimation problem based on the expectation–maximization (EM) algorithm, that is, by fitting the Gaussian mixture model (GMM) centroids that represent a point set (the control point set) and another point set (the observation point set), and regularizing the displacement-field to maintain motion coherence. This design allows us to apply the alignment of two point sets that are not in one-to-one correspondence, and thus provides robustness to data incompleteness, such as noise, outliers, and missing points.

Given these practically useful properties of CPD, a few existing studies have attempted to apply CPD to LA displacement-field estimation [20–22]. In our previous study, we used CPD to estimate subject-specific LA displacement fields over a cardiac cycle from 4D-CT images and proposed using this LA displacement field as a moving-wall boundary condition in computational LA blood flow analysis [22]. Computational approaches to blood flow analysis in the LA in individual patients has attracted attention in the last half decade for assessing the risk of thrombus formation associated with ischemic stroke [22–25]. Thus, a technique such as CPD for estimating a subject-specific LA displacement field from 4D-CT images is desirable, not only for evaluating the LA function, but also for analyzing the internal blood flow characteristics while considering subject-specific LA deformation characteristics. However, the evaluation of the performance of the LA displacement field estimation by CPD has not been sufficient because of a shortage of clinical datasets and quantitative assessments. Thus, the consistency between the estimated results of the LA displacement field obtained by CPD and original LA surfaces extracted from 4D-CT images is unclear. Additionally, CPD involves hyperparameters in its formulation, but their influence on the estimation results has not yet been sufficiently examined.

We assess the performance of CPD-based LA displacement-field estimation taking into account the appropriate setting of hyperparameters. In Section 2, we introduce an outline of the CPD formulation for general readers and describe the workflow of CPD-based LA displacement-field estimation from 4D-CT images. In Section 3, we show the results of CPD parameter adjustment and in Section 4, assess the performance of LA displacement-field estimation over the entire cardiac phase through numerical examples using data from three subjects. We present conclusions in Section 5.

2. Methods

2.1. Outline of coherent point drift

The CPD method proposed in [18] solves the alignment between control point set $\mathbf{X} = \{\mathbf{x}_a \in \mathbb{R}^3 | a = 1 \ldots N\}$ and observation point set $\mathbf{Y} = \{\mathbf{y}_b \in \mathbb{R}^3 | b = 1 \ldots M\}$ to determine the optimal displacement vector of control point set $\mathbf{u} \in \mathbb{R}^{N\times 3}$. For this purpose, CPD assigns the GMM to $\mathbf{X}$ and fits this GMM to $\mathbf{Y}$ using the EM algorithm.

First, a Gaussian distribution with equal isotropic covariances σ^2 is assigned to each control point with a displacement, and thus a probability density function with respect to observation point $p(\mathbf{y}_b|a)$ is given by

$$p(\mathbf{y}_b|a) = \frac{1}{(2\pi\sigma^2)^{\frac{3}{2}}} \exp\left[-\frac{\|\mathbf{y}_b - (\mathbf{x}_a + \mathbf{u}_a)\|^2}{2\sigma^2}\right]. \tag{1}$$

Next, probability density function $p(\mathbf{y}_b)$ of the GMM can be described as the summation form with respect to all control points:

$$p(\mathbf{y}_b) = \sum_{a=1}^{N} P(a) p(\mathbf{y}_b|a), \tag{2}$$

where $P(a)$ is the membership probability and is assumed to be constant ($=1/N$). To account for noise, outliers, and missing points, Eq. (2) is modified by adding uniform distribution $1/M$, given by

$$p(\mathbf{y}_b) = w\frac{1}{M} + (1-w)\sum_{a=1}^{N} \frac{1}{N} p(\mathbf{y}_b|a), \tag{3}$$

where $w \in [0,1]$ is a weighting factor. Following Eq. (3), the negative log-likelihood function $E(\mathbf{u}, \sigma^2)$ can be finally described as

$$\begin{aligned} E(\mathbf{u},\sigma^2) &= -\log \prod_{b=1}^{M} p(\mathbf{y}_b) \\ &= -\sum_{b=1}^{M} \log p(\mathbf{y}_b). \end{aligned} \tag{4}$$

Optimal displacement vector $\mathbf{u}$ and covariance σ^2 are obtained by minimizing E using variational calculus. To avoid overfitting caused by ill-posed conditions, this problem is described as a minimization problem considering L2 (Tikhnov) regulation such that

$$\underset{\mathbf{u}\in\mathbb{R}^{N\times 3}, \sigma^2 \in [0,\infty)}{\text{minimize}} \quad f(\mathbf{u},\sigma^2) = E(\mathbf{u},\sigma^2) + \frac{1}{2}\lambda\|\mathbf{u}\|^2, \tag{5}$$

where λ is a regularization parameter. This minimization problem can be solved using the EM algorithm.

The key idea of the CPD algorithm is to model $\mathbf{u}$ as a Gaussian kernel function to produce a coherent motion of the point set, such that

$$\mathbf{u}_p = \sum_{q=1}^{N} G_{pq}\mathbf{w}_q, \tag{6}$$

where $\mathbf{w} \in \mathbb{R}^{N\times 3}$ is the base function assigned to each control point and $\mathbf{G} \in \mathbb{R}^{N\times N}$ is a kernel matrix with elements

$$G_{pq} = \exp\left(-\frac{\left\|\mathbf{x}_p - \mathbf{x}_q\right\|^2}{2\beta^2}\right), \tag{7}$$

where β is a parameter to determine the span of influence and indices p and q represent nodes in $\mathbf{X}$.

Gaussian kernel matrix $\mathbf{G}$ is a symmetric and positive-define but dense matrix, and thus appropriate compression of $\mathbf{G}$ may be necessary to save computational memory so that CPD can be used in practice. In the original paper [18], this issue was addressed using the low-rank approximation of $\mathbf{G}$ as

$$\begin{aligned} \mathbf{G} &\approx \hat{\mathbf{G}} \\ &= \mathbf{Q}\boldsymbol{\Lambda}\mathbf{Q}^T, \end{aligned} \tag{8}$$

where $\hat{\mathbf{G}}$ is the low-rank approximation of the $\mathbf{G}$, $\boldsymbol{\Lambda} \in \mathbb{R}^{K\times K}$ is a diagonal matrix with the $K(\le N)$ largest magnitude eigenvalues and matrix $\mathbf{Q} \in \mathbb{R}^{N\times K}$ is a set of corresponding eigenvectors. Because it is commonly known that the spectrum of eigenvalues of $\mathbf{G}$ decays quickly, c.f., [26], this technique can sufficiently reduce the computational cost ($K \ll N$).

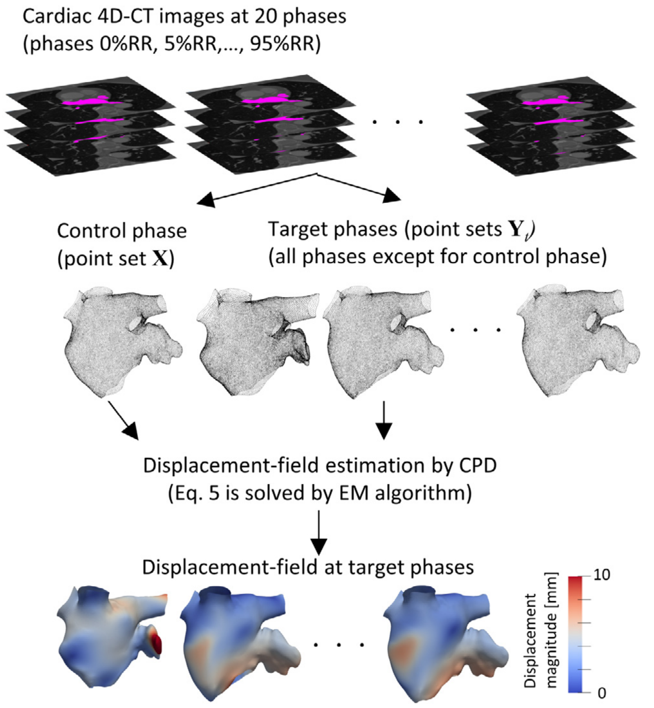

Fig. 1. Workflow of coherent point drift (CPD)-based displacement-field estimation of the left atrium (LA) from 4D-CT images. LA surfaces were reconstructed for a total of 20 phases as sets of triangular elements, and element nodes were used as point sets in the CPD-based displacement-field estimation. The LA surface and its nodes at the phase that maximized the LA surface area were assigned as the control LA surface and control point set **X**, respectively, and the LA surfaces and their nodes at the other 19 phases were assigned as observed LA surfaces and observation point sets $\mathbf{Y}_t$, $t = 1, \ldots, 19$, respectively. The LA displacement field was estimated by solving Eq. (5) at each phase.

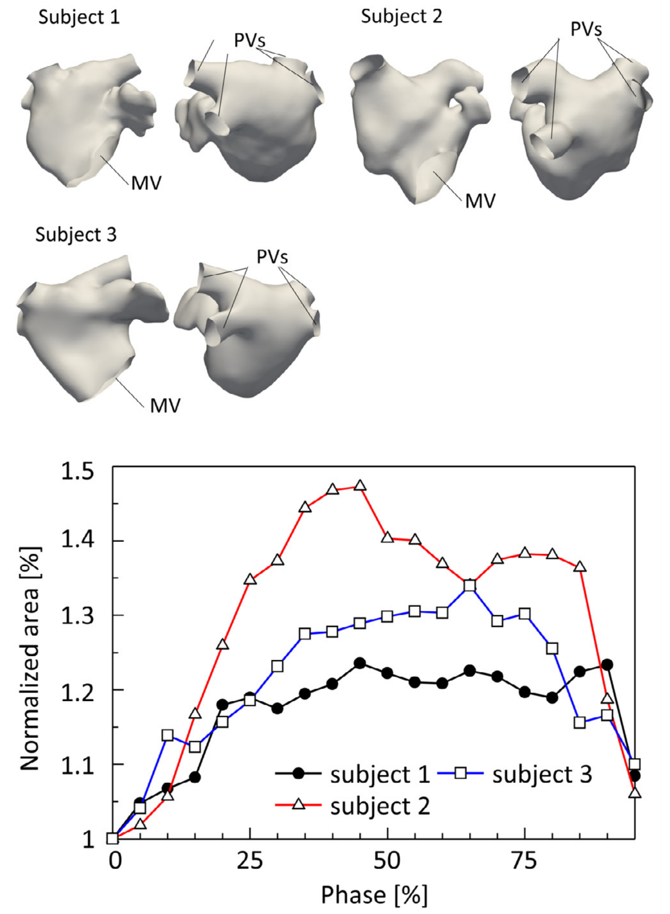

Fig. 2. LA shapes with the maximum surface area during the cardiac phase (top) and time courses of the surface area normalized by the shapes at 0% RR (bottom).

2.2. LA displacement-field estimation from 4D-CT images

Fig. 1 summarizes the workflow for estimating the LA displacement field from 4D-CT images using CPD, following our previous study [22]. The present study uses cardiac 4D-CT images of three subjects without a prior history of cardiac disease (subjects 1, 2, and 3). The protocol was approved by the Institutional Review Board of Jichi Medical University.

The CT images were acquired during normal sinus rhythm using a 128-slice multi-detector CT scanner (SOMATOM Definition Flash, SIEMENS, Inc., Berlin, Germany). The LA outline surfaces were reconstructed for a total of 20 phases (0% RR, 5% RR...95% RR) during the cardiac cycle, where RR indicates the interval of the R waves and 0% RR indicates the electrocardiographic ventricular end-diastole. The reconstructed image matrix size was 512 × 512 × 240 for subject 1, 512 × 512 × 209 for subject 2, and 512 × 512 × 310 for subject 3. The in-plane pixel size was 0.39×0.39 mm^2 for subject 1, 0.41×0.41 mm^2 for subject 2, and 0.52×0.52 mm^2 for subject 3. The through-plane slice thicknesses and slice increments were 1.0 mm for all subjects.

The LA shapes were segmented from images at all phases and LA surfaces were reconstructed by a set of linear triangular elements using the Mimics Medical cardiovascular segmentation tool (Version 21.0.0.406; Materialise, Inc., Yokohama, Japan). The distal part of the PVs beyond the first bifurcation and the MV were removed using MeshMixer (Version 3.5.474; Autodesk, Inc., San Rafael, CA). Fig. 2 shows the LA shapes of all subjects with the maximum LA surface area during the cardiac phase (top) and the LA surface area normalized by it at 0% RR (bottom), which shows that the extent of LA areal changes ranged from 20%–50% in these subjects.

The LA surface and its nodes at the phase when the LA size was largest (65% RR for subject 1, 30% RR for subject 2, and 65% RR for subject 3) were assigned as the control LA surface and control point set **X** because the LA surface shape was relatively clear in whole phases. Those at the other 19 phases were used as the observed LA surface and observation point sets $\mathbf{Y}_t$, $t = 1, \ldots, 19$. The numbers of control point sets were 19,883 for subject 1, 21,294 for subject 2, and 21,826 for subject 3. Additionally, those of observation point sets were 19,215 ± 1,561 for subject 1, 21259 ± 1,215 for subject 2, and 20,673 ± 1,153 for subject 3 (Ave.±S.D.).

Before CPD, the centers of both **X** and $\mathbf{Y}_t$ were set to the origin of the Cartesian coordinate system and their variations were normalized to one. In the computation, we calculated the K largest eigenvalues with the corresponding eigenvectors to obtain the low-rank approximation of **G** in Eq. (8) by the implicitly restarted Arnoldi method implemented in the ARPACK-ng library [27]. Note that outliers were almost eliminated in the LA surface reconstruction process; thus, we assumed these effects were negligible and fixed their weight factor to $w = 0.1$. The computation time needed for displacement-field estimation by CPD was approximately 10 min under parallelization with 12 openMP cores using Intel Xeon E5-2650 (2.20 GHz) processors.

2.3. Evaluations

The effects of hyperparameters β and λ in the CPD formulation and K in the low-rank approximation of **G** on the estimation results were examined via a preliminary computation, as described in Section 3. The global correspondence between the estimated and observed LA shapes was evaluated using the Dice similarity coefficient (DSC) and areal error, which is the difference of LA surface area. The volume overlap between the estimated and observed LA shapes were assessed using the

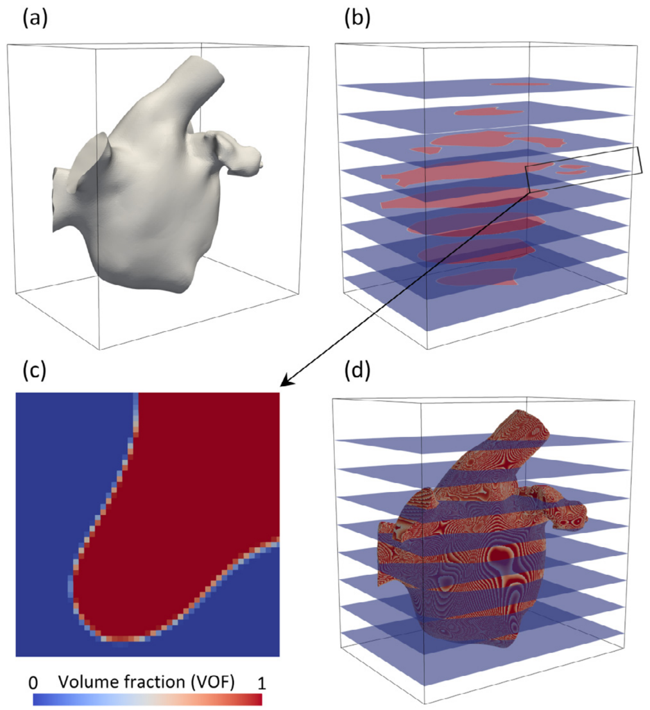

Fig. 3. Flow chart to construct LA volume data in three dimensional (3D) image format. The LA surface shape (a) is projected to the Cartesian grid (b) using volume fraction (VOF) function ϕ, shown in (c). The LA volume is defined as the set of voxels whose VOF is larger than 0.5 (d).

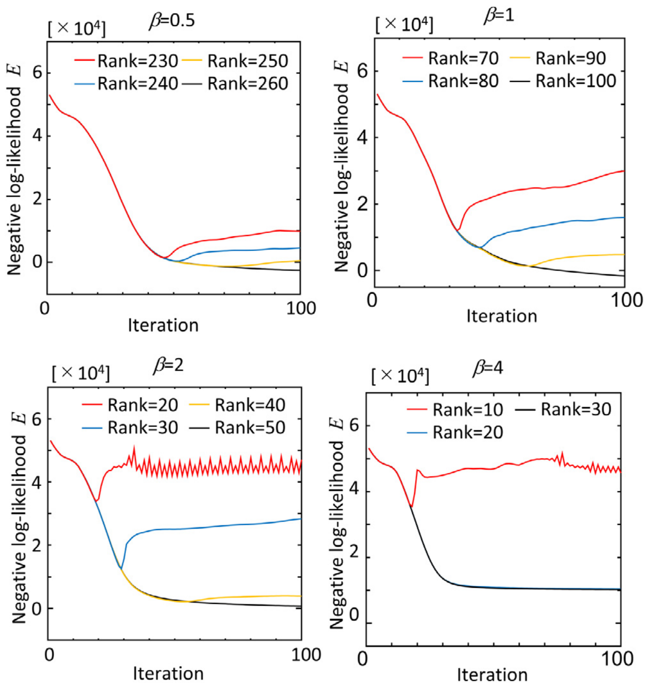

Fig. 4. Profiles of negative log-likelihood E during iterations calculated using a low-rank approximation of Gaussian kernel function $\mathbf{G}$ with $\beta = 0.5$ (top left), 1 (top right), 2 (bottom left), and 4 (bottom right), and the K largest eigenvalues used for the low-rank approximation of $\mathbf{G}$ for the case of subject 1, as representatives.

DSC, which is frequently used for imaging processing. To calculate the DSC from LA surfaces, both the estimated and observed LA surfaces were converted to 3D image data. These LA surfaces were projected into a Cartesian grid with a voxel size of 0.25 mm using the volume fraction (VOF) ϕ $(0 \leq \phi \leq 1)$ (Fig. 3). The VOF function was calculated using open-source software V-SDFlib [28]. Assume that the LA volume consists of a voxel whose VOF is larger than 0.5, and voxels that consist of estimated and observed LA volumes are expressed as the voxel set A and B, respectively. Then DSC is defined as

$$\mathrm{DSC}(A, B) = \frac{2|A \cap B|}{|A| + |B|}. \tag{9}$$

The areal error between estimated and observed LA surfaces is calculated by

$$\text{areal error} = \frac{A^t_{\mathbf{X}}}{A^t_{\mathbf{Y}}} - 1, \tag{10}$$

where $A^t_{\mathbf{X}}$ and $A^t_{\mathbf{Y}}$ are the total surface areas of the estimated and observed LA shapes at phase t, respectively.

In Section 4, in addition to the evaluation of global correspondence, the extent of local correspondences between the estimated and observed LA shapes is assessed using the distances between the estimated and observed LA surface at each cardiac phase point. To calculate the minimum distance between a node of the estimated LA surface $\mathbf{x}_c$ and a triangular element of the observed LA surface, a point on triangular element $\mathbf{x}_p$ is represented by the following linear interpolation:

$$\mathbf{x}_p = (1 - s_p - t_p)\mathbf{x}_{p0} + s_p\mathbf{x}_{p1} + t_p\mathbf{x}_{p2}, \tag{11}$$

where $\mathbf{x}_{p0}$, $\mathbf{x}_{p1}$, and $\mathbf{x}_{p2}$ are the element nodes, s_p and t_p are parameters $(s_p, t_p \geq 0, s_p + t_p \leq 1)$. The minimum distance between $\mathbf{x}_c$ and $\mathbf{x}_p$ is obtained by minimizing $\|\mathbf{x}_p - \mathbf{x}_c\|$ with respect to s_p and t_p.

Finally, we consider the characteristics of the estimated LA surface deformation by assessing the displacement magnitude and its normal (out-of-plane) and tangential (in-plane) components for the estimated LA surface during a cardiac cycle. The magnitudes of the normal and tangential displacement of node a are respectively defined as $\|\mathbf{u}_a \cdot \mathbf{n}\|$ and $\|\mathbf{u}_a - \mathbf{u}_a \cdot \mathbf{n}\|$, where $\mathbf{n}$ is the unit normal vector of the LA surface.

3. Parameter adjustment

We assess the influence of the hyperparameters and low-rank approximation introduced in Section 2.1 on the CPD-based LA displacement-field estimation results. In this assessment, we calculate the displacement-field estimation from the control phase to 0% RR in each subject, which is the phase when the LA size is minimum in a cardiac cycle.

3.1. Influence of the degree of low-rank approximation

The influence of K in the low-rank approximation of $\mathbf{G}$ on the estimation results is visualized by plotting the negative log-likelihood E over the iteration process. Fig. 4 shows the profiles of E for 100 iteration steps using various $\hat{\mathbf{G}}$ with different β(=0.5, 1, 2, and 4) and K for subject 1, as a representative. When $\beta = 2$, for example, E monotonically decayed to the same value regardless of K in the initial stage of the iteration process, whereas an increase of E occurred during the iteration when K was lower than 50. This occurred at an earlier stage of the iteration process when lower values of K were used. Although these tendencies were found in the other cases using different β, the minimum value of K that maintained a monotonic decay of E depended on β. Because the monotonic decay of E is mathematically guaranteed in the EM algorithm, these results indicate that the use of $\hat{\mathbf{G}}$ with values of K that are too small invalidates the mathematical properties of the EM algorithm, which may output inappropriate solutions. Because the minimum acceptable K depends on β, an appropriate K should be selected for each β for each specific problem. In the following sections, we confirm that E monotonically decays during the iteration process when using $\hat{\mathbf{G}}$ for each subject.

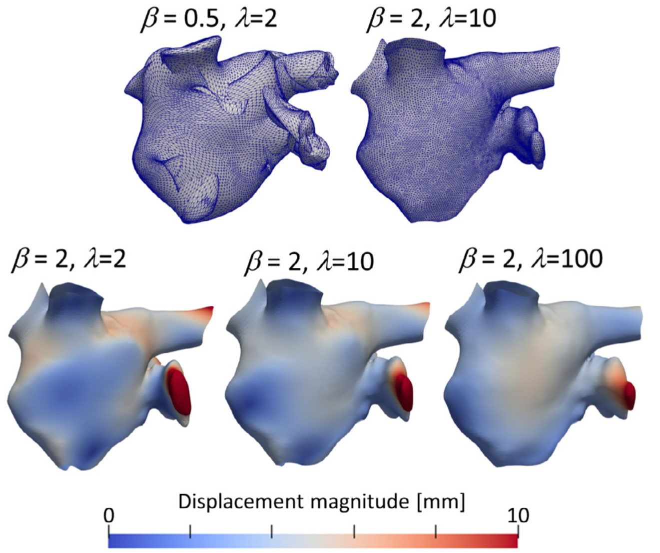

Fig. 5. Representative estimated LA shapes of subject 1 for (β, λ) = (0.5, 2) and (2, 10) (top) and spatial distribution of the areal deformation ratio at 0% RR for (β, λ) = (2, 2), (2, 10), and (2, 100) (bottom).

3.2. Influence of the hyperparameters

We assessed the effects of β and λ on the DSC and the areal error between the estimated and observed LA surfaces using various values for β and λ ($\beta = 0.5$, 1, 2, and 4; $\lambda = 0.5$, 2, 10, 50, and 100).

In the representative case of subject 1 with $\beta = 0.5$ and $\lambda = 2$, unrealistic surface intersections of the LA surface were found in the estimation results because of overfitting (Fig. 5(top)). Because β controls the extent of smoothness of the Gaussian kernel Eq. (7) and λ controls the extent of regularization, small values of β and λ may capture local LA deformation but have a higher risk of overfitting. By contrast, high values of β and λ may overconstrain the LA deformation. Fig. 5 (bottom) shows the displacement of the LA surface of subject 1 for $\beta = 2$ and $\lambda = 2$, 10, and 100 as an example. Although the spatial distributions of the displacement had similar tendencies, these magnitudes decreased as λ increased.

The influence of the hyperparameters β and λ in the CPD algorithm on the LA displacement-field estimation was assessed using the DSC. Fig. 6 shows values of the DSC calculated from the estimated results using various values for β and λ for each subject and their average. Note that several cases, in which the VOF function could not be computed because of surface intersections, are not shown. In all cases in which the VOF could be calculated, the DSC was larger than 0.85 and these ranges were less than 0.08. These results indicate that the internal volume shapes of the estimated and observed LA surfaces successfully overlapped in cases in which the DSC could be calculated. In the cases of $\beta = 0.5$ and 1, surface intersections occurred and the DSC could not be calculated in almost all cases . In the case of $\beta = 2$, the DSC could be calculated in most cases, and these values were nearly constant regardless of λ. In the case of $\beta = 4$, the DSC could be calculated in all cases, and its values decreased as λ increased.

Additionally, the influence of the hyperparameters on the areal error are shown in Fig. 7 for each subject and the average. The areal error decreased as λ increased regardless of β for all subjects. For $\beta = 0.5$ and 1, the areal errors were relatively high (>10%) when λ was small and monotonically decreased as λ increased. For $\beta = 2$ and 4, the decrease of the degree of areal errors became moderate and was in the range ±5%, whereas these values became negative when $\beta = 4$ for all subjects.

Following the above results, we fixed $\beta = 2$ for all subjects for calculation stability and correspondences in terms of the DSC evaluation.

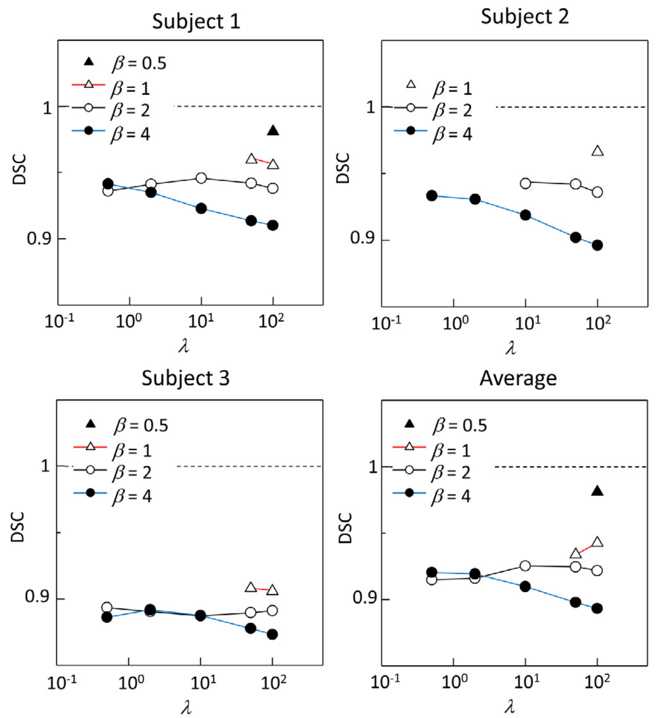

Fig. 6. Effects of β and λ on the Dice similarity coefficient (DSC) between the estimated and observed LA surfaces for subject 1 (top left), subject 2 (top right), subject 3 (bottom left), and average (bottom right). Cases in which the VOF function cannot be computed because of surface intersections are not shown.

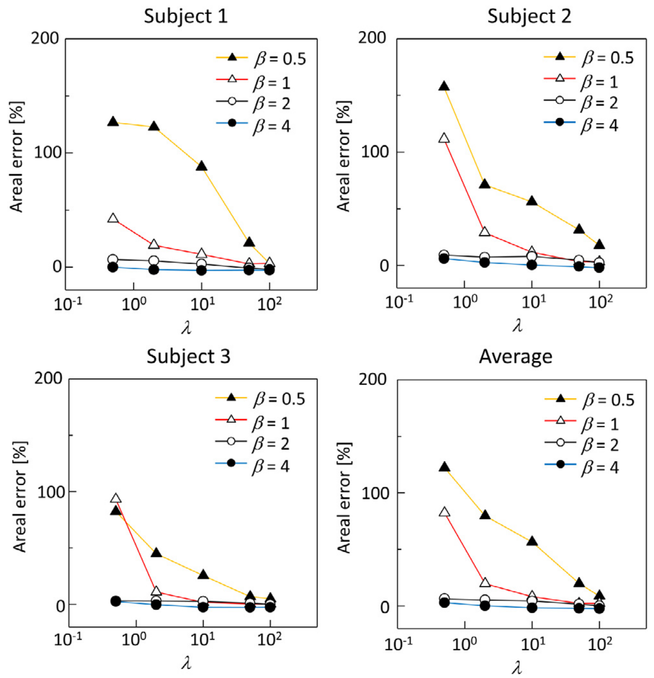

Fig. 7. Effects of β and λ on the areal error between the estimated and observed LA surfaces for subject 1 (top left), subject 2 (top right), subject 3 (bottom left), and average (bottom right).

We also selected the value of λ that minimized the magnitude of areal errors from the above parameter set ($\lambda = 10$ for subject 1, and 100 for subjects 2 and 3).

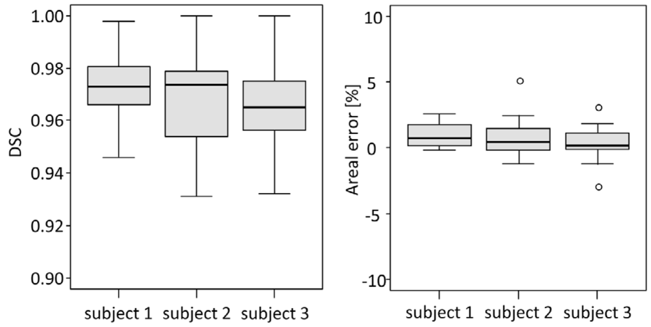

Fig. 8. Box plots of Dice similarity coefficient (DSC) and areal error between the estimated and observed LA surfaces at all phase points.

4. Results and discussion

4.1. Displacement-field estimation

In this section, we reports the results for LA displacement-field estimations for three subjects, which were conducted at 20 cardiac phase points. The parameters β, λ, and K were adjusted by the procedures in Section 3.

The global correspondence of the LA surfaces of the estimated and observed LA shapes was confirmed by the DSC and areal error over a whole cardiac cycle (Fig. 8). The values of the DSC were higher than 0.92 and the areal ratio was less than ±5%, including outliers, for all subjects. These results show that the LA shapes estimated by CPD globally fit the observed LA shapes well.

Fig. 9 shows representative snapshots of the observed and estimated LA shapes with distances from the observation over a cardiac cycle. The entire time courses of these LA shapes over a cardiac cycle are shown in the supplementary movies S1, S2, and S3 for subjects 1, 2, and 3, respectively. For all subjects, unrealistic intersections were not found at all phase points. Surface distances were locally high in the boundary domains of the PVs and mitral annulus (MA; junction between the LA and LV) in the whole cardiac phase and the LAA, particularly at the LA systole phases (e.g., Fig. 9 (top center)). Because boundaries at the PVs and MA cannot be defined explicitly in CT images and CT resolution is still insufficient to capture the LAA structure, particularly at the LA systole phase, these regions in the observed LA shapes may be incomplete, that is, with missing or false detections. In the estimated results, the displacement field of these regions was interpolated based on surrounding point displacements, and then locally and temporally high surface distances may have been caused in estimation results.

A quantitative assessment of the surface distances between the observed and estimated LA surfaces was conducted for each subject. Fig. 10 shows the distributions of surface distances in each cardiac phase without the outliers found in the boundary domains and LAA, as shown in Fig. 9. For subject 1, distances mainly ranged from 0 mm to 1.5 mm and these medians were less than 0.5 mm at all phases. For subjects 2, distances ranged from 0 mm to 2 mm and medians were less than 0.5 mm at all phases except for phase 95% RR, at which the median was approximately 0.6 mm. These tendencies were also found for subject 3. Because the slice thickness of the CT images of all subjects was 1 mm, we believe that the surface distances observed are acceptable for tracking the LA shape from the 4D-CT images with current spatial resolutions.

Finally, we considered the deformation characteristics of the LA surface based on the LA displacement field estimated using CPD. Fig. 11 shows spatial distributions of the displacement magnitude of the LA surface, and its normal and tangential components at phase 0% RR, which was the maximum contraction phase for each subject. The displacement magnitude was highest at the LAA region, whereas the displacement of the superior–posterior side of the LA among the PVs (i.e., the atrial roof) was relatively lower than that of other sides for all subjects. These relatively lower displacements were also found in *in vivo* measurements in [29] using speckle tracking echocardiography.

The magnitudes of the normal and tangential components of the displacement were comparable, but their spatial distributions showed different characteristics (Fig. 11 (middle and bottom)). The normal displacement was relatively high on the superior–anterior side of the LA for all subjects, whereas the tangential displacement was relatively high on the LAA and inferior side of the LA. It is commonly known that the atrial roof is nearly fixed in the cardiac phase, but the MA cyclically moves along the LV longitudinal axis while maintaining its circular shape in a cardiac cycle [30]. Thus, passive LA deformation associated with the MA motion may cause relatively larger tangential displacement in the inferior side of the LA. These findings suggest that estimated global LA deformation is qualitatively consistent with common clinical knowledge and highlights the necessity of using a spatial displacement-field estimation approach to express subject-specific LA deformation, which includes local anisotropic properties.

4.2. Limitations

The displacement-field estimation conducted in this study has four limitations. First, the extent of local LA displacements depends on hyperparameters β and λ, as shown in Fig. 5(bottom), but it is currently difficult to select the most appropriate values. Because the LA shape is not explicitly represented in the CT images, to date, there is no methodology that can identify the kinematically exact solution from the displacement-field estimation. Although we believe that the present workflow is sufficiently robust to estimate the global LA displacement field, this limitation should be carefully handled in the quantitative assessment of the LA displacement field, particularly in local regions. Second, the effects of CT artifact and segmentation errors on the accuracy of the observation LA shapes were not considered when the CPD parameters were set. We tuned the parameters to fit the estimated LA shape well to the observed LA shape. However, cardiac CT imaging is influenced by motion artifacts [31] and its spatial resolution is still too low to capture a complex and dynamic LAA structure, particularly in the LA systole, and thus the observed LA surfaces contain errors that originate from the CT scanning, segmentation, and reconstruction processes. This influence on the estimated results in terms of the distance between the estimated and observed LA surfaces are shown in Appendix A. Because of this limitation, the assessment of differences in estimated LA displacement within a few voxels should be also carefully treated. Third, this study used the original CPD algorithm [18], but several improved versions of the CPD have been proposed. There are many ideas to improve the CPD algorithm because of its outstanding performance and high extensibility [32–36]. For example, these modifications have achieved automatic parameter optimization for adjusting noise and outliers [33], and used landmark points and a prescribed structure [32,36]. Although these updates necessitate an additional optimization routine and input information, an improved CPD may help us to obtain suitable results more easily. Fourth, the workflow used in this study does not consider temporal interpolation of the LA displacement field, even though 4D-CT imaging outputs sequential volumetric data. In the present workflow, the control point set was fixed and subsequent displacement-field estimation was independently conducted for each phase. Overcoming this drawback may enable us to obtain spatiotemporally reasonable LA motions from the 4D-CT images, which has good potential to not only directly apply the estimation results to the moving wall boundary in the CFD simulation but also improve our physiological knowledge of LA functions.

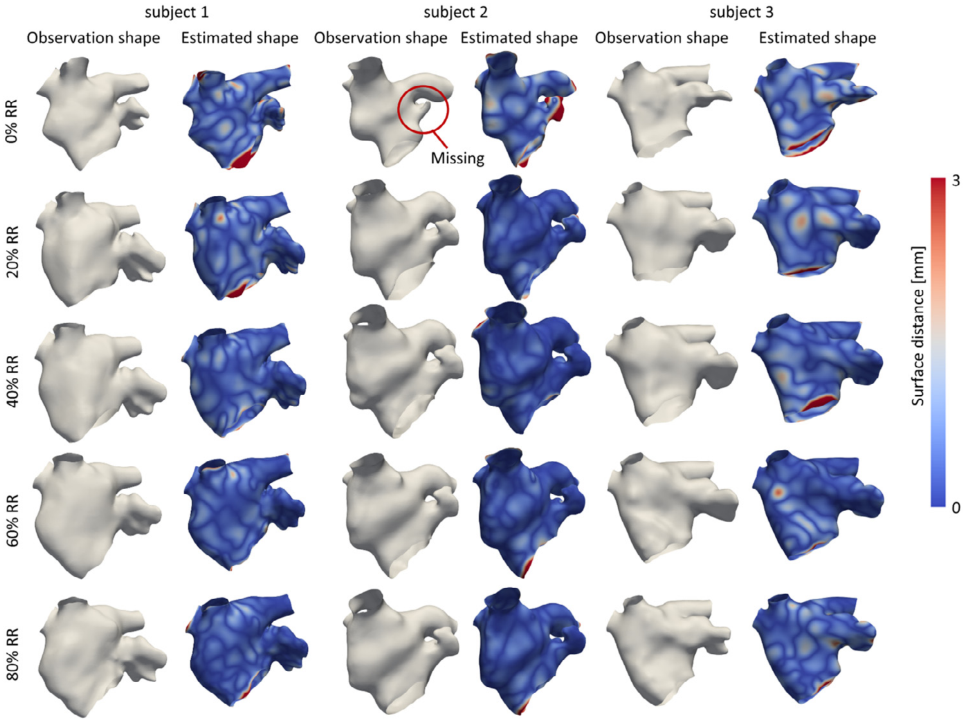

Fig. 9. Representative snapshots of observed LA shapes and estimated LA shapes with surface distances from the observation for subjects 1 (left), 2 (center), and 3 (right) at phases 0% RR, 20% RR, 40% RR, 60% RR, and 80% RR.

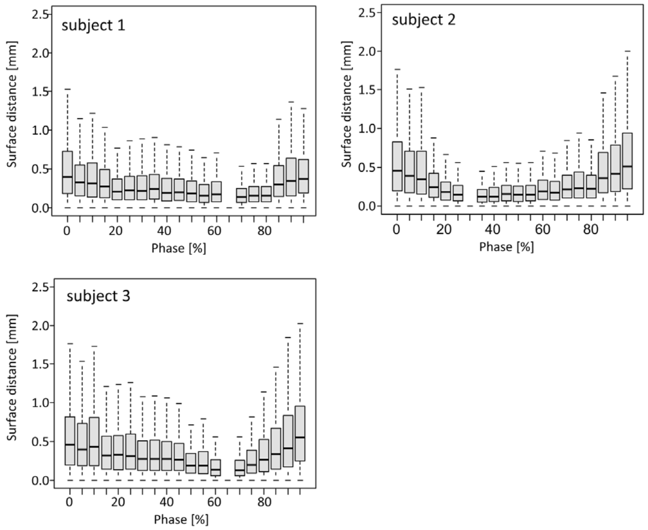

Fig. 10. Box plots of the distances between the estimated and observed LA shapes at all phase points. Note that outliers are not included in these plots.

5. Conclusions

In this study, we investigated the performance of CPD-based LA displacement-field estimation using cardiac 4D-CT images with the appropriate parameter settings. These results demonstrate that the estimated LA displacement field successfully tracked the observed LA shapes reconstructed from 4D-CT images with interpolated incomplete regions over a cardiac cycle. Furthermore, the estimated LA deformation characteristics with local anisotropy were consistent with existing clinical observations. These results highlight the quality of the performance and validity of the CPD-based workflow in terms of estimating global LA displacement fields that are consistent with the LA surface deformation extracted from 4D-CT images. This achievement reinforces the validity of existing studies [20,22] and will help readers to conduct LA deformation estimation and analysis smoothly. Furthermore, assessments of the influence of each hyperparameter on LA displacement estimation illustrated the parameter sensitivities and current limitations of the proposed approach. Thus, this knowledge may be valuable for readers who attempt to adjust hyperparameters for not only LA surface displacement estimation but also their specific problem.

Finally, a sequential LA displacement field over a cardiac cycle obtained using this framework may be useful not only for the subject-specific assessment of the LA function but also for computational LA blood flow analysis that considers clinically consistent LA deformation characteristics. We hope that this technique will help to improve our understanding of the LA function and its internal blood flow characteristics.

Declaration of competing interest

The authors have no financial or personal interests in the work reported in this paper.

Acknowledgments

We thank Kazunori Yamakoshi for the 4D-CT data acquisition, and Naoki Takeishi, Shunichi Ishida and Taiki Shigematsu for fruitful discussions. We also thank the reviewers for their constructive comments. This work was supported by research grants from JSPS Grants-in-Aid for Scientific Research (18K0876) and MEXT, Japan as "Priority Issue on Post-K computer (supercomputer Fugaku)" (Integrated computational life science to support personalized and preventive medicine) (hp180202 and hp190187). We thank Kimberly Moravec, Ph.D., and Maxine Garcia, Ph.D., from Edanz Group (www.edanzediting.com/ac) for editing a draft of this manuscript.

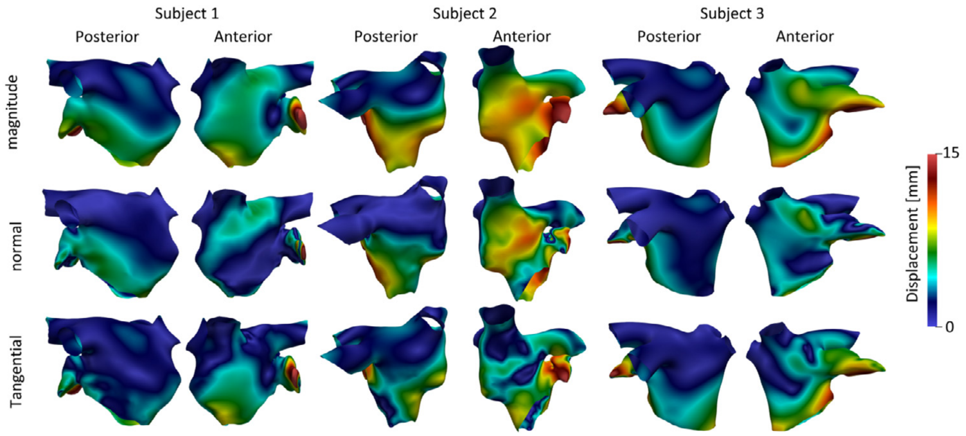

Fig. 11. Spatial distributions of the displacement magnitude (top) and its normal (middle) and tangential (bottom) components against the left atrial (LA) surface in the estimation results at the maximum contraction phase for each subject: posterior (left) and anterior (right) views.

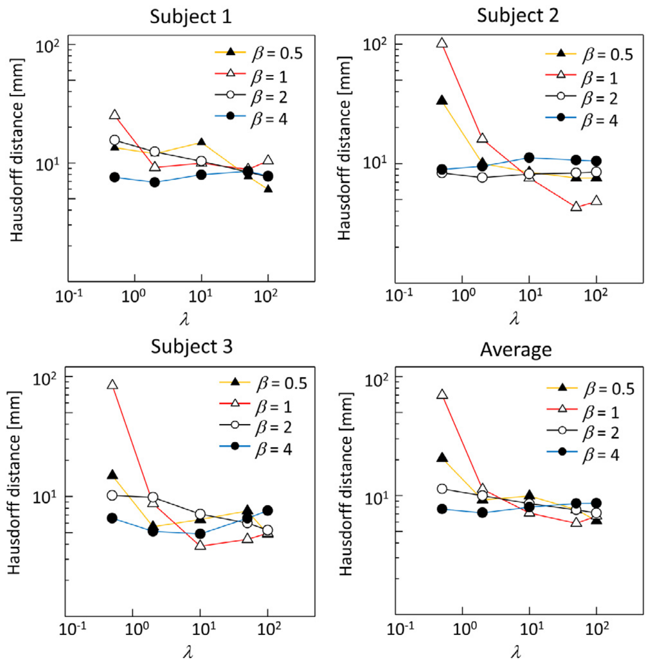

Fig. A.1. Effects of β and λ on the Hausdorff distance between the estimated and observed LA surfaces for subject 1 (top left), subject 2 (top right), subject 3 (bottom left), and average (bottom right).

Appendix A. Hausdorff distance between the estimated and observed LA surfaces

To consider the distance between the estimated and observed LA surfaces, we calculated the Hausdorff distances between these point sets. The Hausdorff distance between the point sets of the estimated and observed LA surfaces **X** and **Y**, respectively are defined as

$$\text{Hausdorff distance}\,(\mathrm{X}, \mathrm{Y}) = \max_{\mathbf{x}\in\mathrm{X}} \min_{\mathbf{y}\in\mathrm{Y}} \|\mathbf{x} - \mathbf{y}\|\,, \tag{A.1}$$

where **x** and **y** is the position vectors of the point involved in **X** and **Y**, respectively.

The influence of the hyperparameters β and λ in the CPD algorithm on the LA displacement-field estimation was assessed using the Hausdorff distance, as in Section 3. Fig. A.1 shows the Hausdorff distances calculated from the estimated results using various values for β and λ for each subject and their average. Although there were a few cases with relatively long distances (>50 mm) at $\lambda = 0.5$, and $\beta = 0.5$ and 1 for each subject, certain values ranged from 5 to 10 mm in most cases, regardless of the hyperparameters. Because the Hausdorff distance is equivalent to the maximum value of surface distances (Fig. 9), we believe that the values of the Hausdorff distance are determined by the incompleteness of the observed LA surface rather than the influence of the hyperparameters.

Appendix B. Supplementary data

Supplementary material related to this article can be found online at https://doi.org/10.1016/j.compbiomed.2019.103454.

References

[1] B.D. Hoit, Left atrial size and function: Role in prognosis, J. Am. Coll. Cardiol. 63 (6) (2014) 493–505, http://dx.doi.org/10.1016/j.jacc.2013.10.055.

[2] P.A. Wolf, R.D. Abbott, W.B. Kannel, Original contributions atrial fibrillation as an independent risk factor for stroke: The Framingham study, Stroke 22 (8) (1991) 983–988, http://dx.doi.org/10.1161/01.STR.22.8.983.

[3] E.J. Benjamin, R.B. D'Agostino, A.J. Belanger, P.A. Wolf, D. Levy, Left atrial size and the risk of stroke and death : The Framingham heart study, Circulation 92 (4) (1995) 835–841, http://dx.doi.org/10.1161/01.CIR.92.4.835.

[4] Y.Y. Inoue, A. Alissa, I.M. Khurram, K. Fukumoto, M. Habibi, B.A. Venkatesh, S.L. Zimmerman, S. Nazarian, R.D. Berger, H. Calkins, J.A. Lima, H. Ashikaga, Quantitative tissue-tracking Cardiac magnetic resonance (CMR) of left atrial deformation and the risk of stroke in patients with atrial fibrillation, J. Am. Heart Assoc. 4 (4) (2015) e001844, http://dx.doi.org/10.1161/JAHA.115.001844.

[5] B. Desjardins, E.A. Kazerooni, ECG-gated Cardiac CT, Am. J. Roentgenol. 182 (4) (2004) 993–1010, http://dx.doi.org/10.2214/ajr.182.4.1820993.

[6] A. Frangi, W. Niessen, M. Viergever, Three-dimensional modeling for functional analysis of cardiac images: a review, IEEE Trans. Med. Imaging 20 (1) (2001) 2–25, http://dx.doi.org/10.1109/42.906421.

[7] V. Tavakoli, A.A. Amini, A survey of shaped-based registration and segmentation techniques for cardiac images, Comput. Vis. Image Underst. 117 (9) (2013) 966–989, http://dx.doi.org/10.1016/j.cviu.2012.11.017.

[8] A. Sotiras, C. Davatzikos, N. Paragios, Deformable medical image registration: a survey, IEEE Trans. Med. Imaging 32 (7) (2013) 1153–1190, http://dx.doi.org/10.1109/TMI.2013.2265603.

[9] J. Huang, D. Abendschein, V.G. Dâvila-Român, A.A. Amini, Spatio-temporal tracking of myocardial deformations with a 4-D B-spline model from tagged MRI, IEEE Trans. Med. Imaging 18 (10) (1999) 957–972, http://dx.doi.org/10.1109/42.811299.

[10] E. McVeigh, C. Ozturk, Imaging myocardial strain, IEEE Signal Process. Mag. 18 (6) (2001) 44–56, http://dx.doi.org/10.1109/79.962277.

[11] J. Sra, D. Krum, A. Malloy, M. Vass, B. Belanger, E. Soubelet, R. Vaillant, M. Akhtar, Registration of three-dimensional left atrial computed tomographic images with projection images obtained using fluoroscopy, Circulation 112 (24) (2005) 3763–3768, http://dx.doi.org/10.1161/CIRCULATIONAHA.105.565218.

[12] J. Sra, S. Ratnakumar, Cardiac image registration of the left atrium and pulmonary veins, Heart Rhythm 5 (4) (2008) 609–617, http://dx.doi.org/10.1016/j.hrthm.2007.11.020.

[13] R. Beigel, N.C. Wunderlich, S.Y. Ho, R. Arsanjani, R.J. Siegel, The left atrial appendage: Anatomy, function, and noninvasive evaluation, JACC Cardiovasc. Imaging 7 (12) (2014) 1251–1265, http://dx.doi.org/10.1016/j.jcmg.2014.08.009.

[14] Y. Zheng, D. Yang, M. John, D. Comaniciu, Multi-part modeling and segmentation of left atrium in C-Arm CT for image-guided ablation of atrial fibrillation, IEEE Trans. Med. Imaging 33 (2) (2014) 318–331, http://dx.doi.org/10.1109/TMI.2013.2284382.

[15] C. Jin, J. Feng, L. Wang, H. Yu, J. Liu, J. Lu, J. Zhou, Left atrial appendage segmentation and quantitative assisted diagnosis of atrial fibrillation based on fusion of temporal-spatial information, Comput. Biol. Med. 96 (2018) 52–68, http://dx.doi.org/10.1016/j.compbiomed.2018.03.002.

[16] H. Chui, A. Rangarajan, A new point matching algorithm for non-rigid registration, Comput. Vis. Image Underst. 89 (2–3) (2003) 114–141, http://dx.doi.org/10.1016/S1077-3142(03)00009-2.

[17] B. Amberg, S. Romdhani, T. Vetter, Optimal step nonrigid ICP algorithms for surface registration, in: IEEE Conference on Computer Vision and Pattern Recognition, IEEE, 2007, pp. 1–8, http://dx.doi.org/10.1109/CVPR.2007.383165.

[18] A. Myronenko, X. Song, Point set registration: Coherent point drifts, IEEE Trans. Pattern Anal. Mach. Intell. 32 (12) (2010) 2262–2275, http://dx.doi.org/10.1109/TPAMI.2010.46.

[19] G.K.L. Tam, Z.-Q. Cheng, Y.-K. Lai, F.C. Langbein, Y. Liu, D. Marshall, R.R. Martin, X.-F. Sun, P.L. Rosin, Registration of 3D point clouds and meshes: a survey from rigid to nonrigid, IEEE Trans. Vis. Comput. Graph. 19 (7) (2013) 1199–1217, http://dx.doi.org/10.1109/TVCG.2012.310.

[20] M. Koch, A. Kleinoeder, F. Bourier, J. Hornegger, N. Strobel, Novel method for comparison of pre-planned ablation lines for treatment of atrial fibrillation using a common reference model, IEEE 10th International Symposium on Biomedical Imaging (2013) http://dx.doi.org/10.1109/ISBI.2013.6556405.

[21] M. Koch, S. Bauer, J. Hornegger, N. Strobel, Towards deformable shape modeling of the left atrium using non-rigid coherent point drift registration, in: H.P. Meinzer, T. Deserno, H. Handels, T. Tolxdorff (Eds.), Bildverarbeitung Für Die Medizin 2013. Informatik Aktuell, Springer, Berlin, Heidelberg, 2013, pp. 332–337, http://dx.doi.org/10.1007/978-3-642-36480-8_58.

[22] T. Otani, A. Al-Issa, A. Pourmorteza, E.R. McVeigh, S. Wada, H. Ashikaga, A computational framework for personalized blood flow analysis in the human left atrium, Ann. Biomed. Eng. (44) (2016) 3284–3294, http://dx.doi.org/10.1007/s10439-016-1590-x.

[23] R. Koizumi, K. Funamoto, T. Hayase, Y. Kanke, M. Shibata, Y. Shiraishi, T. Yambe, Numerical analysis of hemodynamic changes in the left atrium due to atrial fibrillation, J. Biomech. 48 (3) (2015) 472–478, http://dx.doi.org/10.1016/j.jbiomech.2014.12.025.

[24] M. Nuñez-Garcia, T. De Potter, E. Silva, O. Camara, G. García-Isla, A.L. Olivares, H.G. Morales, X. Freixa, J. Noailly, C. Butakoff, D. Sanchez-Quintana, Sensitivity analysis of geometrical parameters to study haemodynamics and thrombus formation in the left atrial appendage, Int. J. Numer. Methods Biomed. Eng. 34 (8) (2018) e3100, http://dx.doi.org/10.1002/cnm.3100.

[25] G.M. Bosi, A. Cook, R. Rai, L.J. Menezes, S. Schievano, R. Torii, G. Burriesci, Computational fluid dynamic analysis of the left atrial appendage to predict thrombosis risk, Front. Cardiovasc. Med. 5 (April) (2018) 1–8, http://dx.doi.org/10.3389/fcvm.2018.00034.

[26] F.R. Bach, M.I. Jordan, Kernel independent component analysis, J. Mach. Learn. Res. 3 (1) (2003) 1–48.

[27] ARPACK-ng library, https://github.com/opencollab/arpack-ng.

[28] V-SDFlib, https://vcad-hpsv.riken.jp/en/release_software/VSDFlib/.

[29] T.F. Cianciulli, M.C. Saccheri, J.A. Lax, A.M. Bermann, D.E. Ferreiro, Two-dimensional speckle tracking echocardiography for the assessment of atrial function, World J. Cardiol. 2 (7) (2010) 163, http://dx.doi.org/10.4330/wjc.v2.i7.163.

[30] M. Carlsson, H. Mosén, M. Ugander, T. Buhre, H. Arheden, Atrioventricular plane displacement is the major contributor to left ventricular pumping in healthy adults, athletes, and patients with dilated cardiomyopathy, Am. J. Physiol.-Heart Circ. Physiol. 292 (3) (2006) H1452–H1459, http://dx.doi.org/10.1152/ajpheart.01148.2006.

[31] K. Kalisz, J. Buethe, S.S. Saboo, S. Abbara, S. Halliburton, P. Rajiah, Artifacts at Cardiac CT: Physics and solutions, RadioGraphics 36 (7) (2016) 2064–2083, http://dx.doi.org/10.1148/rg.2016160079.

[32] Y. Hu, E.-J. Rijkhorst, R. Manber, D. Hawkes, D. Barratt, Deformable Vessel-Based Registration Using Landmark-Guided Coherent Point Drift, Springer, 2010, pp. 60–69, http://dx.doi.org/10.1007/978-3-642-15699-1_7.

[33] P. Wang, P. Wang, Z.G. Qu, Y.H. Gao, Z.K. Shen, A refined coherent point drift (CPD) algorithm for point set registration, Sci. China Inf. Sci. 54 (12) (2011) 2639–2646, http://dx.doi.org/10.1007/s11432-011-4465-7.

[34] Y. Gao, J. Ma, J. Zhao, J. Tian, D. Zhang, A robust and outlier-adaptive method for non-rigid point registration, Pattern Anal. Appl. 17 (2) (2014) 379–388, http://dx.doi.org/10.1007/s10044-013-0324-z.

[35] S. De Sousa, W.G. Kropatsch, Graph-based point drift: Graph centrality on the registration of point-sets, Pattern Recognit. 48 (2) (2015) 368–379, http://dx.doi.org/10.1016/j.patcog.2014.06.011.

[36] L. Peng, G. Li, M. Xiao, L. Xie, Robust CPD algorithm for non-rigid point set registration based on structure information, PLoS One 11 (2) (2016) 1–17, http://dx.doi.org/10.1371/journal.pone.0148483.